Multidirectionally Patterned Interdigital Transducers for Enhancing Acoustofluidic Streaming with Flexible Printed Circuit Board

Mercedes Stringer, Povilas Dumčius, Xiaoyan Zhang, Yanyan Chai, Ziming Zeng, Zhiqiang Dong, Chao Sun, Dongfang Liang, Guangbo Ge, Yongqing Fu, Zhenlin Wu, and Xin Yang*

Acoustic streaming generated by surface acoustic waves (SAWs) enables diverse acoustofluidic functions, such as fluid mixing, particle manipulation, and enhanced fluid transport, making SAWs valuable lab-on-a-chip systems. However, conventional SAW devices are often limited to a specific acoustofluidic function once fabricated. Each function typically requires different devices or designs to produce other wave modes, making exploration costly and time-consuming. A Multidirectional Interdigital Transducer (M-IDT) on a Flexible Printed Circuit Board (FPCB) is presented, allowing easy reconfigurability and multidirectional SAW propagation. This versatile device enables rapid, multifunctional experimentation on a single replaceable substrate, facilitating efficient exploration of acoustofluidic effects. This device, alongside finite element simulations, investigates substrate in-plane rotation angles (0°, 30°, 60°, and 90° relative to the X-axis) and wave modes. Favorable acoustic velocities are observed using Rayleigh SAW (R-SAW) at 0° and 30°, and using combined wave modes at 60°, and 90°. The pseudo shear-horizontal SAW (P-SH-SAW) at 90° exhibits higher velocities than R-SAW at 0°. P-SH-SAW also improved acoustic streaming at lower power, with high-viscosity fluids, substantial fluid volumes (1 mL), and within a 96-well plate. The M-IDTs reconfigurable nature allows rapid, cost-effective testing, making it ideal for prototyping a wide range of acoustofluidic applications.

1. Introduction

SAWs, particularly those generated by applying radio-frequency (RF) signals to IDTs, have gained significant attention in the field of acoustofluidics. Compared to bulk acoustic waves (BAWs), SAWs offer greater flexibility and precision for small-scale operations, while BAWs excel in high-throughput applications.[1] These devices offer versatile manipulation of bioparticles and fluids, miniaturization capability, and compatibility with other sensing/microfluidic components, making them ideal for lab-on-a-chip and biomedical applications.[2–7] Typically, Rayleigh SAW (R-SAW) propagating along the X-axis on a 128° YX-cut lithium niobate (LiNbO$_3$) substrates are employed for acoustofluidic functions,[8] due to their significant surface normal displacement, which facilitates efficient energy and momentum transfer to fluids.[9] As a result, these devices are widely used for acoustofluidic functions such as mixing, pumping, concentrating, and

M. Stringer, P. Dumčius, X. Zhang, Y. Chai, Z. Zeng, X. Yang
Department of Electrical and Electronic Engineering
School of Engineering
Cardiff University
Cardiff CF24 3AA, UK
E-mail: yangx26@cardiff.ac.uk

Z. Dong
International Joint Laboratory of Biomedicine and Engineering
College of Biomedicine and Health
College of Life Science and Technology
Huazhong Agricultural University
Wuhan 430070, P. R. China

C. Sun
School of Life Sciences
Northwestern Polytechnical University
Xi'an 710072, P. R. China

D. Liang
Department of Engineering
University of Cambridge
Cambridge CB2 1PZ, UK

G. Ge
Shanghai Frontiers Science Center of TCM Chemical Biology
Institute of Interdisciplinary Integrative Medicine Research
Shanghai University of Traditional Chinese Medicine
1200 Cailun Road, Shanghai 201203, P. R. China

Y. Fu
Faculty of Engineering and Environment
Northumbria University
Newcastle Upon Tyne, Newcastle NE1 8ST, UK

Z. Wu
School of Optoelectronic Engineering and Instrumentation Science
Dalian University of Technology
Dalian 116023, P. R. China

**ADVANCED
SCIENCE NEWS**

www.advancedsciencenews.com

**ADVANCED
FUNCTIONAL
MATERIALS**

www.afm-journal.de

jetting.[10] However, conventional LiNbO₃ substrates are limited in the range of acoustic wave modes they can generate once the crystal cut and electrode patterns are defined.[11,12] This limitation often confines conventional SAW devices to a single function per device, requiring different geometries or designs to achieve additional wave modes.[13] Exploring and developing substrates with diverse orientations on a single device could open new possibilities for functionalities and applications.

The ability to generate waves on a substrate in a multidirectional manner offers substantial advantages in acoustofluidics.[8] For instance, the use of multidirectional SAWs for acoustic tweezers, such as two orthogonal symmetric standing SAWs,[1,14] enables the creation of intricate 2D patterns for cell separation,[15,16] and single cell analysis.[14,17,18] Additionally, incorporation of travelling SAWs (TSAWs) for levitation in a third direction allows for the realization of 3D acoustic tweezers.[19] Another acoustic tweezer configuration using symmetrical tri-directional IDTs generates TSAWs to achieve programmable control microparticle movements.[20] These straightforward approaches offer rapid, precise, and noncontact control over particles and cells,[17] making it suitable for diverse biomedical applications including tissue engineering, in vitro cell studies, or 3D biometric structures. Understanding SAW phenomena, particularly with IDTs at different angles on anisotropic substrates, is crucial for determining subsequent acoustofluidic effects.[9] Research effort has been made to explore R-SAW phenomena under various setups, shedding light on practical considerations for optimal transducer designs.[9] This understanding becomes paramount when considering the interaction of SAWs with the fluidic environment, as it enables the mitigation of adverse effects and optimization of acoustic streaming for enhanced micro- and nanoparticle manipulation.[8,21]

Moreover, simultaneous excitation of multiple wave modes,[11,22] such as shear-horizontal SAWs (SH-SAWs) and R-SAWs, has shown promise in enhancing biosensor sensitivity and overcoming diffusion limitations without causing particle damage.[13,23] Such SH-SAW biosensors hold significant potential for the detection of[24] DNA[25] and proteins[26] in liquid environments. Although both fluidic and sensing functions have been realized effectively on various crystal cuts, the integration of SH-SAW for acoustofluidic actuation applications remains relatively unexplored,[11,27,28] mainly due to its reduced damping effects or weakened coupling with the liquid. The promising result of dominant SH-SAWs on alternative crystal cuts, such as 36° YX-cut LiTaO₃ substrate, underscore its suitability for acoustofluidic applications requiring mixing, pumping, and jetting.[27,28] For instance, SH-SAW generated on 36° YX-cut LiTaO₃ achieved streaming velocities of 5 mm s⁻¹, exceeding those of R-SAW on the same substrate, which produced 2 mm s⁻¹ for 2 μL water droplet at 15 dBm.[27] It is noteworthy that the SH-SAW streaming velocity on 36° YX-cut LiTaO₃ is comparable in magnitude to that observed on standard R-SAW produced on the 128° YX-cut LiNbO₃ substrate with a similar size and power.[27,29] Additionally, SH-SAWs have also been demonstrated to induce vertical jetting,[28] presenting valuable tools for applications such as 2D and 3D bioprinting, needle-free fluid injection, and single-molecule detection. While 36° YX-cut LiTaO₃ is effective for SH-SAW applications, 128° YX-cut LiNbO₃ is widely preferred for R-SAWs due to its superior electromechanical coupling and

energy transfer. Thin-film materials like AlN and ZnO offer flexibility and thermal stability, but have reduced piezoelectric performance.

This paper introduces using a multidirectional device, consisting of a FPCB IDT, which allows the study of multidirectional wavefields. This reconfigurable platform supports rapid investigations and offers greater versatility compared to conventional IDTs. Despite advancements with multidirectional wavefields and wave modes, a comprehensive investigation of wave modes and angles remains largely unexplored. Our team demonstrated that alternating the in-plane rotation angle relative to the X-axis on the 128° YX-cut LiNbO₃ substrate enabled a synergistic blend of R-SAW and SH-SAW mechanisms for rapid exosome concentration.[30] Building on this, the current study explores the role of complex wavefields in optimizing acoustofluidic device performance. By refining angle and wave mode selection, we reveal the potential to unlock multiple acoustofluidic effects within a single device. The M-IDTs adaptable design provides a flexible platform for researchers, allowing quick prototyping and efficient testing. While the M-IDT system in this study focuses on prototyping and testing different wave modes and angles, its reconfigurable design offers potential for integrating multiple acoustofluidic functions, such as mixing, concentration, and jetting, on a single platform. This versatility opens new possibilities for exploring a wide range of acoustofluidic applications with greater ease and precision.

2. Working Mechanism

The reconfigurable and multidirectional M-IDT was developed using the 128° YX-cut LiNbO₃ substrate to explore multi-mode acoustic excitation. The M-IDT leverages its geometry and reconfigurability to generate wave propagation at multiple angles, enabling access to wave modes that would otherwise be challenging with a single-directional IDT. The design features six trapezoidal interdigital electrodes (IDEs) arranged in a hexagonal configuration, enabling the study of acoustic streaming at in-plane rotation angles 0°, 30°, 60°, and 90° relative to the X-axis (**Figure 1a**). This device enables a comprehensive exploration of wave modes and acoustic interactions across multiple directions, and its reconfigurable design allows for the investigation of additional angles or even different substrates.

The M-IDT consists of a mechanical jig that integrates several key components: a base plate that supports the entire device, a rigid PCB component that connects the FPCB to the SMA connectors, an aluminum ring that secures the whole structure to the base plate, localized pressors that apply the clamping force, silicon pads that evenly distribute the clamping force, and M5 screws that generate the clamping pressure. The mechanical jig ensures precise contact between the FPCB IDT and the LiNbO₃ substrate while facilitating easy connections to the system setup, including power supplies. Additionally, matching network are connected to the rigid PCB via SMAs to optimize power transfer.

The M-IDT device can be easy reconfigured by loosening the screws on the aluminum ring to allow manual rotation of the LiNbO₃ substrate, guided by a circular paper template that indicated the angles. In this study, angles are defined relative to the reference flat on the LiNbO₃ substrate: at 0° in-plane rotation angle, the reference flat is perpendicular to the center of the IDE
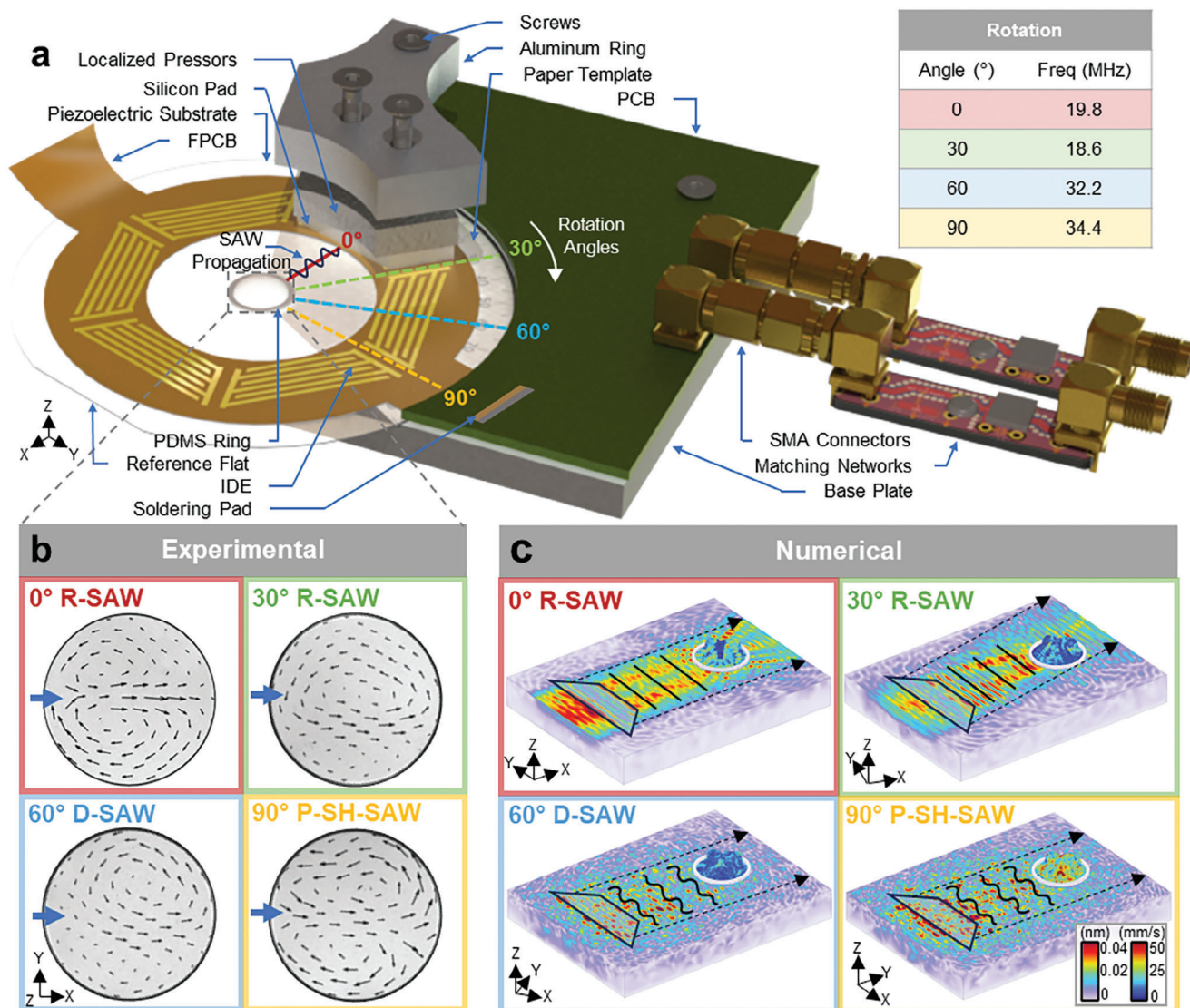
Figure 1. Overview of the multidirectional system. The figure illustrates a) the M-IDT device, b) the experimental droplet streaming at various rotation angles and wave modes, and c) 3D numerical results corresponding to these angles and wave modes. The top right corner provides a color coded key for the rotation parameters, detailing the applied angles and frequencies.

(as shown in Figure 1a), while at 30°, it is rotated 30° relative to the X-axis. Two configurations were used: one with the reference flat at 0°, with the other IDEs positioned at 60° intervals, and another with the reference flat rotated by 30°, achieving a 90° orientation for the other IDEs. While the IDTs are fixed at 60° intervals, rotating the substrate relative to the IDTs allows the testing of intermediate angles, such as 30° and 90°. Although the manual process requires a brief adjustment period, this design simplifies fabrication and replacement which enables rapid investigations into acoustic streaming, making it a valuable tool for both fundamental research and practical applications.

At each angle, different wave modes are generated by adjusting the frequency applied to the IDT, producing unique combinations of wave modes.[6] At 0° in-plane rotation, the R-SAW mode predominates, characterized by significant surface displacement and a high coupling coefficient, making it effective for acoustic

streaming, as shown in Figure 1b,c. At 30°, a modified R-SAW mode emerges, influenced by substrate anisotropy, with altered phase velocity and attenuation properties. The 60° rotation generates a Dual-SAW (D-SAW) mode,[30] which combines surface and shear-horizontal waves, overing a complex interaction beneficial for applications requiring a balance wave characteristics.[30] At 90°, the P-SH-SAW mode is observed, which, like D-SAW, merges surface and shear-horizontal waves but with a higher coupling coefficient, achieving comparable streaming velocities to the R-SAW at 0°. The P-SH-SAW's performance is analyzed in terms of its damping effects across various fluid viscosities, power levels, and vessel sizes/types.

The distinct streaming patterns produced by these wave modes at 0°, 30°, 60°, and 90° (Figure 1b) are useful for understanding the underlying acoustofluidic mechanisms. Each angle and wave mode result in different patterns that reflect the distribution of

**ADVANCED
SCIENCE NEWS**

www.advancedsciencenews.com

**ADVANCED
FUNCTIONAL
MATERIALS**

www.afm-journal.de

acoustic energy within the fluid. These patterns are influenced by power flow angles and wave propagation characteristics.

Simulations (Figure 1c) confirm the experimental findings, helping to identify the optimal angles and wave modes for specific angles. This detailed analysis enhances our understanding and contributes to the optimization of acoustic streaming SAW technologies. The results highlight the potential of alternative wave modes, like P-SH-SAW, for applications such as particle manipulation in viscous fluids, opening new avenues for biomedical applications. This research enhances the possibilities for advanced acoustic streaming manipulation and sensing in fields such as biomedicine and industrial processes.

SAWs are mechanical waves that propagate along the surface of a piezoelectric substrate, with their energy concentrated within a one-wavelength-thick waveguide just below the surface.[31,32] These waves comprise a combination of longitudinal and shear waves and have an elliptical motion in the plane defined by the direction of wave propagation and normal to the substrates surface.[6,31]

The propagation characteristics of SAWs are strongly influenced by the crystal structure of the substrate material.[31,32] In anisotropic materials, where properties vary with direction, the behavior of SAW propagation can significantly differ depending on the orientation of the crystal or substrate axes relative to wave direction.[31]

Key parameters that characterize SAW behavior include phase velocity, coupling coefficient, and beam steering.[9] Understanding and measuring these parameters are important for optimizing the performance of SAW devices, as they directly influence the efficiency and behavior of the acoustic waves.[8,21] Among these, the coupling coefficient and beam steering are particularly important:[9] they determine how effectively the device converts electrical energy into acoustic energy and how the wave energy is directed, respectively.[9,32]

The coupling coefficient is the numerical measure of conversion efficiency between electrical and acoustic energy in a piezoelectric material.[8] It is calculated using the following equation,

$$K^2 = 2\frac{v_f - v_m}{v_f} \tag{1}$$

where v_f and v_m are the SAW phase velocities, calculated for free (no electrode) and electrically short-circuits surface (with electrode), respectively.[33] The coupling coefficient is a good indicator of piezoelectric material performance.[7]

Beam steering refers to the phenomenon where the wave phase does not propagate in the same direction as the wave energy.[7] This effect is closely related to the power flow angle (ψ), which is the angle between the direction of wave propagation and the beam direction (given by the power flow).[9] The power flow angle is a key parameter in determining beam steering and is calculated by:

$$\psi = tan^{-1}\left(\frac{1}{v}\frac{dv}{d\theta}\right) \tag{2}$$

where dv is the change in mode velocity caused by a change in $d\theta$ (radians) in its propagation direction on a plate face, and ψ (radians) is an angle between a mode beam and a propagation

direction.[33] Different wave modes and substrate orientation will produce unique power flow angles,[33] thereby influencing the degree of beam steering.

By carefully considering these parameters- coupling coefficient and power flow angle-, one can enhance device performance, ensuring desired acoustofluidic effects are achieved within a single device.

3. Experimental Section

3.1. Device Fabrication and Assembly

The assembly of the M-IDT involved the purpose-built mechanical jig facilitating contact between the FPCB IDE and the substrate (abstract illustration shown in Figure 1a). An aluminum base plate, circular paper template, and 128° YX-cut LiNbO₃ wafer were carefully positioned and aligned to ensure correct substrate angles. The rigid PCB was securely fastened with the screws, and the FPCB IDEs were pressed against the substrate using localized pressers and silicon pads, held by an aluminum ring clamp. The flexible nature of the FPCB-IDT compensates for surface roughness and ensures consistent contact without requiring evenly distributed pressure. To maintain reproducibility, the clamping force was optimized by monitoring the S_{11} parameter using a vector network analyzer (VNWA). This method allows for consistent assembly by identifying the optimal force for minimum S_{11} values, as demonstrated in previous studies.[36,37] The assembly was completed with the addition of a polydimethylsiloxane (PDMS) ring to provide consistent fluid boundary and placement. For these experiments, the PDMS ring was centered within the M-IDT setup to ensure uniform wave propagation. Note that the DMS ring's position can be easily adjusted, providing flexibility for future experiments to explore its effects on wave propagation and interaction. A detailed description of the device fabrication and assembly is in the Supporting Information (SI), which shows an exploded view of the SolidWorks assembly (Figure S1a, Supporting Information), a cross-section schematic (Figure S1b, Supporting Information), and a fully assembled real-life model (Figure S1c, Supporting Information). The six IDEs were placed in a hexagonal-shaped configuration which allowed for trapezoidal-shaped IDEs. Simulations indicate that this shape could enhance acoustic beam width and facilitate uniform wavefields (Figure S2a, Supporting Information) compared to a rectangular IDE. The design of the M-IDT is shown in Figure S2b (Supporting Information), displaying the six IDEs and the bus bars to connect the electric potential and ground. Figure S2c (Supporting Information) shows a photograph of one of the trapezoidal IDEs with insert displaying a microscope image of the electrode fingers. The IDT fabrication involved FPCB and rigid PCB, offering versatility, ease of replacement, and cost-efficiency. Previous studies demonstrated the effectiveness of PCB- and FPCB-based IDTs for generating SAWs.[36–38] FPCB-based IDTs were chosen for their versatility, as they can be easily replaced, redesigned, or used with different substrate materials, making them ideal for prototyping. Their flexibility ensures consistent contact even with dimensional variations, allows lifting unused IDTs to minimize reflections, and reduces manufacturing cost and effort compared to cleanroom-made devices, while also offering better heat dissipation and

dynamic flexing capabilities. Further descriptions of the design and fabrication of the M-IDT are in the Supporting Information.

3.2. Device Operation

The acoustofluidic system integrates system controls, electrical characterization, the M-IDT platform, and data collection and analysis, as illustrated in Figure S3 (Supporting Information). The system operates by actuating IDTs using RF signals to generate SAW for acoustic streaming.

The system controls involve RF signal generation from signal generators (RS Pro, RSDG 5162) and are amplified with a power amplifier (Mini circuit, LZY-22+). Input signals to the IDTs are monitored via power meters (Keysight 8990B) connected to a coupler (Mini-circuit, ZFBDC20-62HP-S+), allowing real-time efficiency calculations from the forward and reverse powers. The difference between forward and reverse power is used to determine the effective power for SAW conversion, and any significant drop in efficiency (e.g., below 10 dBm) triggers a system check to prevent damage.

Electrical characterization of the system was performed using S-parameters, which measure how RF signals are transmitted and reflected. The key parameter, S_{11} represents the reflection coefficient, with its minima indicating the resonant frequencies/wave modes where minimal power is reflected, thus maximizing power transfer. These measurements were conducted using a vector network analyzer (DG8SAWQ) (VNA, E5061B ENA, Keysight Technologies, U.K.), with the M-IDT connected via SMA connectors. The S_{11} minima were monitored when fastening the screws to secure the substrate so that there were optimal minima's whilst avoiding substrate damage.

Characterization of the 128^0 XY-cut LiNbO$_3$ involved measuring S_{11} minima across a frequency sweep from 15 to 40 MHz. This range was selected as it captured the largest S_{11} minima's and over 20 wave modes for analysis. Measurements were taken at angles from 0° to 90° in 5° increments, with alignment ensured by a circular paper template. Each measurement was repeated five times for precision.

The M-IDT, central to the acoustofluidic platform, was placed under a microscope (GX Vision Ltd, GXM-L2800) equipped with an overhead camera to capture images and videos of the acoustofluidic streaming within the PDMS ring. This setup enabled data collection and analysis which provided visual documentation.

A matching network was designed using an LC circuit to improve power transferred to the IDTs and address impedance mismatching. In higher power applications, impedance mismatching can lead to significant issues such as inefficient power transfer and increased signal reflection, which reduces the effective power available for SAW generation and damages to the signal generator. The matching network consists of inductors (L) and capacitors (C) configured to match the IDT impedance to the source, improving power transfer and reducing signal reflection. The measured S-parameters guided the tuning of the LC components, which led to increased S_{11} minima, signifying enhanced power transfer. Although matching networks are typically unnecessary for clean room IDTs, they are beneficial for PCB-based IDTs, where the mechanical clamping can reduce power trans-

mission efficiency.[38] For exploratory experiments, the matching network is not strictly necessary, as it is frequency-dependent and tailored for specific operating conditions. During initial testing at various angles and frequencies, the matching network was not used to allow rapid testing and reconfiguration. Once the operating frequency and angle are determined, a matching network can be individually optimized to ensure maximum performance. An example matching network and its design process is described in the SI and shown in Figure S4 (Supporting Information).

3.3. Particle Solution Preparation

Red 10 µm polystyrene particles (Sigma Aldrish, USA) were used to visualize the acoustic streaming flow fields in different experimental setups. These particles were diluting in various glycerol-water ratios and 100 µL of the mixture was added to a PDMS ring. For the angle-frequency experiments, a 1:100:100 ratio of particles, water, and glycerol, was used for clear visualization[39] and analysis of the acoustic streaming patterns using computer software (PIVLAB).[40,41] In the viscosity experiments, the water-glycerol ratios were adjusted to represent varying viscosities. The mixtures included a 100:0 (water: glycerol) ratio for the least viscous condition, followed by 80:20, and lastly 60:40 to mimic the viscosity of body fluids at room temperature.[42] For the varying power (20,27,30 dBm) and large volume (1 mL) experiments, a consistent 60:40 (water: glycerol) ratio was used. Lastly, in the single 96-well culture plate experiments, the same particle ratio was used, but with 300 µL of fluid in each well.

3.4. Data Analysis

The mathematical software MATLAB supplied a particle image velocimetry tool (PIVlab),[40,41] which was adopted to analyze the velocity field. This non-invasive technique was used to calculate the flow field information based on moving images recorded from the microscope on the overhead camera.

3.5. Numerical Simulation

This study employed finite element modelling techniques using COMSOL Multiphysics (v5.5) to investigate SAW, focusing on IDTs fabricated on 128^0 XY-cut LiNbO$_3$ substrate. The numerical studies were conducted to explore, visualize, and calculate wave mode data generated at different angles and frequencies. Three models are presented: Model 1, a 3D periodic unit cell IDT (Figure S5, Supporting Information); Model 2, a simplified 3D IDT (Figure S6, Supporting Information); and Model 3, a life-scale 2D IDT (Figure S7, Supporting Information). Each model incorporated specific geometries, boundary conditions, and meshing. Additionally, different analysis techniques were used, such as eigenfrequency and frequency studies to calculate the piezoelectric, pressure acoustics, and laminar flow properties. These models collectively offered a comprehensive understanding of SAW behavior under various conditions, providing insights into wave modes, vibration patterns, and interactions with external factors like droplets. Each model addresses specific
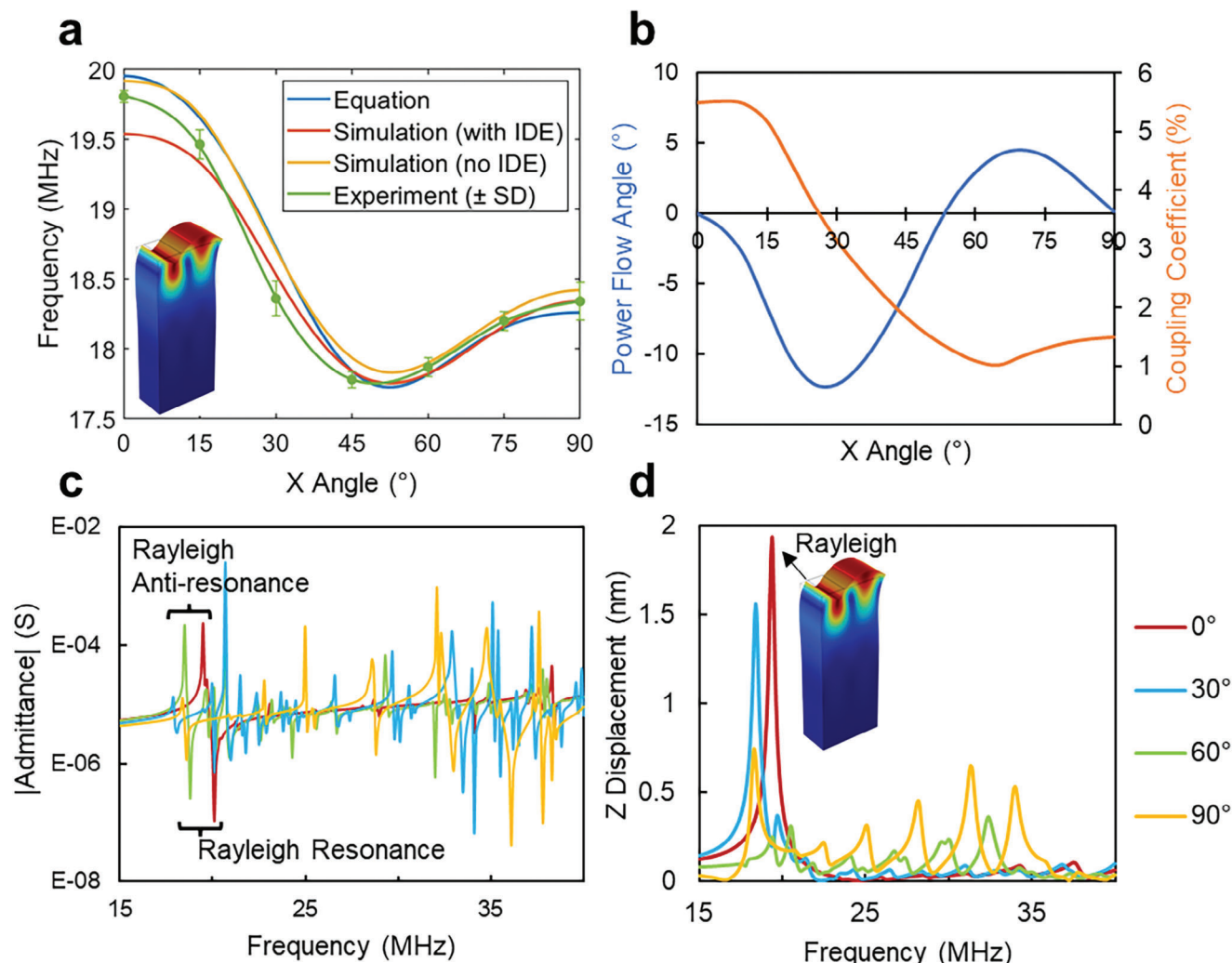
ADVANCED
SCIENCE NEWS
www.advancedsciencenews.com

ADVANCED
FUNCTIONAL
MATERIALS
www.afm-journal.de

Figure 2. Eigenfrequency simulation results showing a) R-SAW Frequency at various rotation angles, validated by Equation (3) and experimental S_{11} measurements ($n = 5$). The experimental data is represented as mean ± s.d. b) Calculated R-SAW coupling coefficient and power flow angle at various angles. c) Absolute admittance showing other modes. c) Z displacements on a single point on the surface of the IDT.

needs: Model 1 captures wave modes but lacks fluid interactions, Model 2 simulates wavefield patterns with simplified geometry, and Model 3 shows real-scale streaming but is limited to 2D. Together, they provide a comprehensive understanding of SAW behavior. Detailed information on each model setup and methodology is in the SI.

4. Results and Discussion

4.1. Numerical Analysis

Numerical studies of a single unit IDT (Figure S5, Supporting Information) provided fundamental information on the excitation of SAW for different in-plane rotation angles relative to the X-axis. **Figure 2a** shows the simulated eigenfrequency results for R-SAWs at various angles around the X-direction, for free (no IDE) and electrically short-circuits surface (with IDE). In the presence of the IDE, resonant behavior is observed, driven by the periodicity of the IDEs. Without the IDE, the resonant frequency

is instead influenced by the periodicity given to the substrate's width, which defines the SAW wavelength. This behavior is consistent with the wavelength-to-frequency relationship $v = \lambda f$. The phase velocity, in both cases, is determined by the substrate's material properties and the orientation of wave propagation. The obtained values match well with the experimental reading of the R-SAW, derived from the measured S_{11} minima, and are consistent with the predictions from the following continuous fourth-order Fourier series:[21]

$$v(\theta) = a_0 + \sum_{n=1}^{n=4} a_n \cos(n\omega\theta) + b_n \sin(n\omega\theta) \tag{3}$$

where the fitted parameters are given in Table S1 (Supporting Information).[21] It should be noted that the simulated eigenfrequency values are lower with IDEs placed on top of the substrate compared to without using IDEs. The difference is caused by the resonance frequency not being equivalent to the synchronous frequency of the IDE because the internal reflections at the electrodes caused an asymmetry of resonance peaks of the reflection

**ADVANCED
SCIENCE NEWS**

www.advancedsciencenews.com

**ADVANCED
FUNCTIONAL
MATERIALS**

www.afm-journal.de

coefficient. Hence, the resonance frequency was slightly lower in these cases than the synchronous frequency.[9] Additionally, the differences between the simulated frequency values and experimental values were caused by differing phase velocities since the phase velocity within the IDT differs from that of uncoated LiNbO$_3$ due to the presence of electrode metallization.[9]

The simulated eigenfrequency values were used to find the R-SAW phase velocities for free and electrically short-circuited surfaces. These phase velocities enabled the calculation of the coupling coefficient and power flow angles using Equations (1) and (2), respectively. As shown in Figure 2b, the calculated coefficient and power flow angles for R-SAW at various in-plane rotations with respect to the X-axis show excellent agreement with values reported in the literature,[8,9,21] and the simulated wavefields shown in Figure S8 (Supporting Information). For instance, propagation along the X-axis ($\theta = 0°$) demonstrated a coupling coefficient of 5.5% and the two lines of symmetry at $\theta = 0°$ and $\theta = 90°$.[43]

The observed variation in both the coupling coefficient and power flow angle suggests opportunities for further experimentation. Specifically, at a 30° rotation, the R-SAW coupling coefficient was moderately reduced to 3.2%, with a significant variation in the power flow angle to $-12.1°$. This indicated a notable change in the energy distribution and directionality of the wave, potentially useful for tuning device performance. Conversely, the results also highlight instances where the R-SAW has poor coupling, such as ~60° rotation, where the coupling coefficient dropped to 1%. While this reduction may limit the effectiveness of such configurations for practical applications, it also provides valuable insights into optimizing device designs where high coupling characteristics are desired. This concept extends beyond R-SAW, as exploring other wave modes[33] opens further possibilities for performance enhancement. For example, one study demonstrated how anisotropy and higher order wave modes could be used to improve the performance of liquid sensors.[43] This highlights the potential of using both anisotropy- through control of coupling coefficients and power flow angles- and other wave modes to optimize SAW devices for specific purposes.

Other wave modes, in addition to R-SAW, exist and can be visualized through the admittance of the system. Admittance (the reciprocal of impedance) quantifies how easily the electrical signal is transmitted through the piezoelectric substrate by the IDTs. It provides insight into the electrical behavior and resonances of the system. The simulated admittance graphs at 0°, 30°, 60°, and 90° rotations of the IDTs are shown in Figure 2c. Each peak in the admittance graph corresponds to a distinct resonance in the system, which represents a different acoustic wave mode. The number of peaks indicated the number of modes detected at a given rotation angle. The total modes detected in one substrate may be as large as ≈100.[33] However different modes have different effects on a fluid; some of these wave modes could generate fluidic streaming valuable for acoustofluidic applications. Traditionally, R-SAW has been favored for acoustofluidic actuation due to its effective energy transfer to fluids.[9] Whereas, SH-SAWs have been used as an effective fluid biosensor due to its minimal damping or attenuation in fluid, making them less effective for fluid actuation.[13,27,44] Hence for these wave modes found, further evaluation needs to be considered.

While admittance can predict the existence of modes, additional criteria such as Z displacement is useful for evaluating the practical abilities in acoustofluidics. For large Z displacement values there is significant surface normal displacement, which facilitates efficient energy and momentum transfer to the fluid and hence shows the potential wave modes that may allow fluid streaming.[9] The simulated Z displacement on a singular point of the unit model is shown in Figure 2d. The largest Z displacement is ≈0.9 nm for 0° R-SAW at 19.8 MHz. The next largest Z displacement is the R-SAW for 30°, and 90°. The 60° R-SAW has a low Z displacement which correlates well with the coupling coefficient in Figure 2b. Interestingly, there are other Z displacements at higher wave modes, such as 90° at ≈34.4 MHz, though with a smaller Z displacement of ≈40% compared to 0° R-SAW, is still worth investigating.

Moreover, all the simulated wave modes between 15 MHz and 40 MHz were plotted with respect to the X-direction, as shown in **Figure 3a**. The Mode 0 (red) is identified as the R-SAW wave mode, distinguished by its characteristic phase velocity with varying angle. In contrast, other acoustic wave modes, e.g., the bulk waves inside the substrate, are excited at higher frequencies, resulting in greater phase velocities. Note that each wave mode and its calculated properties are shown in the SI Figures S9 and S10 (Supporting Information).

These surface waves have three mechanical displacement components: two shear and one longitudinal displacement (Vertical shear Z-component, longitudinal X-component, and horizontal shear Y-component as annotated in pink on Figure 3b).[45] Each wave mode has a mixture of each component, which may vary depending on the rotation angle. The numerical analysis accounts for all three physical features of wave propagations in anisotropic crystals.[45] For example, Figure 3b illustrates the wave mode shapes of the first three modes in Figure 3a at 0°, 30°, 60°, and 90° rotation angle, highlighting the interaction of the three mechanical displacement components. Mode 0 distinctly shows the surface wave component of R-SAW, while Mode 1 (Leaky-SAW) demonstrates the penetration of the surface wave component into the substrate bulk. Mode 2 encompass shear-horizontal components that propagate on the surface and in the bulk.

As the rotation angle varies, the wave mode shapes changes. At 30° and 60° rotation, substantial alteration in wave mode shapes is observed, with the appearance becoming less structured compared to the 0° rotation, despite some resemblance. At 90° rotation, minimal changes in mode shapes occur compared to 0°, although a slight shift is noticeable. This demonstrates that wave modes exhibit hybrid characteristics, offering potential advantages for exploitation.

The coupling coefficient and power flow angle were calculated with respect to frequency for different in plane X rotations (0°, 30°, 60°, and 90°) to visualize the characteristics for each angle. The simulated S_{11} values show a good correlation with the coupling coefficient (**Figure 4**), indicating that the S_{11} is a useful metric for assessing the conversion efficiency from electrical to acoustic energy. A lower S_{11} minimum signifies a reduced electrical reflection to the signal generator, thereby enhancing energy used for SAW excitation, while a higher S_{11} minimum suggests an impedance mismatch. It should be noted that the low S_{11} values are attributed to simulation limitations related to the unit cell

**ADVANCED
SCIENCE NEWS**

www.advancedsciencenews.com

**ADVANCED
FUNCTIONAL
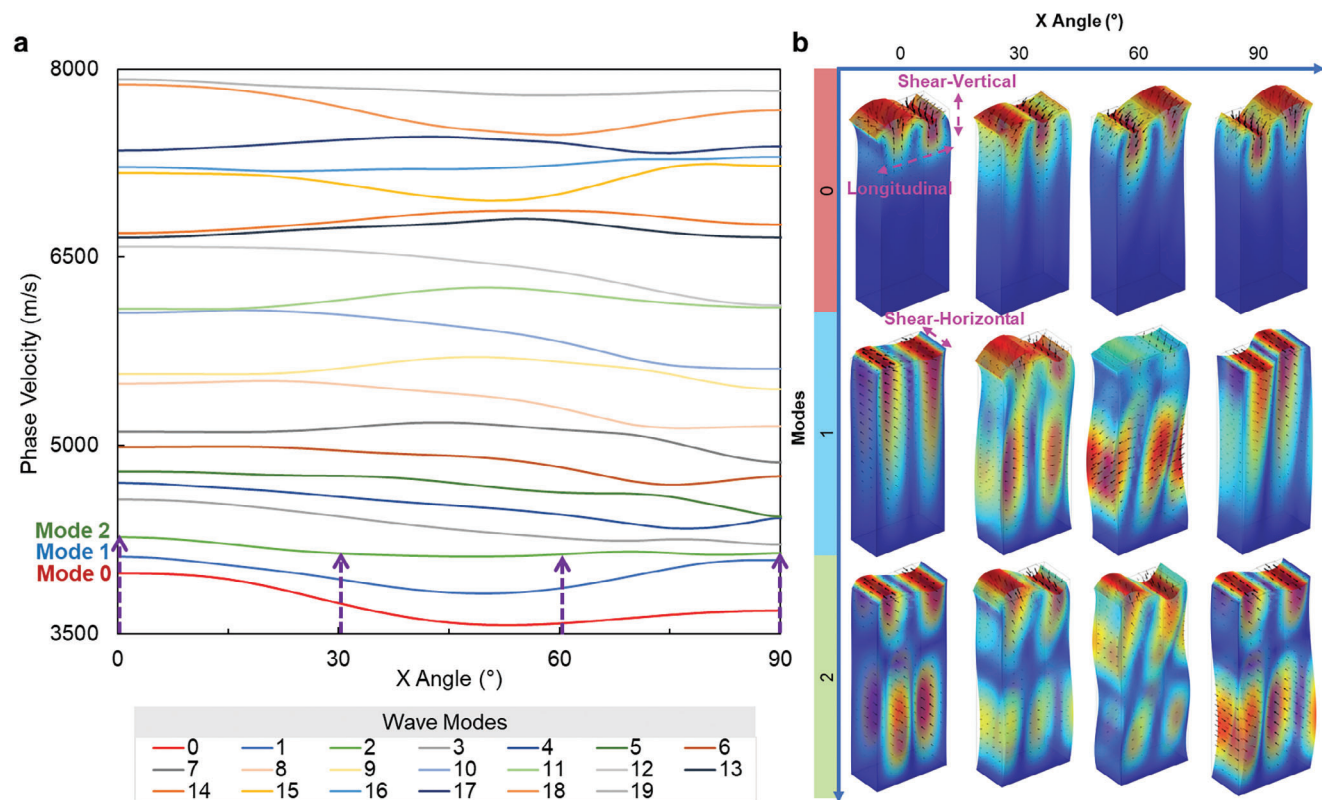MATERIALS**

www.afm-journal.de

Figure 3. Simulated wave modes. a) Wave modes with respect to rotation angles b) Three simulated wave mode shapes (modes 0 to 2) at 0°, 30°, 60°, and 90° rotation angle.

thickness. Further details, including S_{11} values for various unit cell thicknesses, are provided in Figure S11 (Supporting Information).

At 0° (Figure 4a), the R-SAW mode has the highest coupling coefficient (≈5.5%), with a corresponding low S_{11} minimum, indicating optimal energy conversion efficiency. The power flow angle is near zero, consistent with theoretical predictions, which ensures stable and predictable device behavior. This makes the 0° R-SAW mode a highly favorable choice for efficient SAW device performance.

In contrast, at 30° (Figure 4b), the R-SAW mode (18.6 MHz) shows a moderate coupling coefficient (≈2%), with a significant power flow angle of ≈ 12.1°. Although this is less efficient than the 0° R-SAW orientation, the larger power flow angle may offer enhanced wave steering capabilities, which could be advantageous in applications requiring directional control of acoustic waves. Another mode at 20.5 MHz has a similar coupling coefficient but with a smaller power flow angle (−2.2°). This variability in power flow angle suggests that while 30° may not be as efficient as at 0° and introduce complex wave behavior, it provides flexibility in wave steering and multi-mode operation.

The 60° rotation (Figure 4c) has a moderate coupling coefficient at 33.5 MHz with a power flow angle of −2.2°. These results are similar to the 30° case; however, this higher frequency mode may involve other wave mode components, leading to potential challenges in device design. Despite this, the 60° orientation could be valuable in applications where these wave modes are desired, offering a balance between efficiency and functional

versatility. For instance, our team successfully utilized the 60° rotation at 32.8 MHz (Dual-SAW) for nano-scale exosome concentration, leveraging the multi-mode capability.[30]

At 90° (Figure 4d), the coupling coefficient remains relatively high (≈5.1%) at 35.2 MHz, with a near-zero power flow angle, similar to 0° rotation. This suggests that 90° is also an efficient orientation for energy conversion, with direct energy propagation. The higher frequency at this angle might involve other wave mode components, which could affect fluidic streaming efficiency depending on the wave's interaction with the liquid medium.

It should be noted that at higher frequencies, the simulated wave modes show more irregularities, most likely due to having more crossovers in frequencies or a smaller mesh size needed. Additionally, the power flow calculations could be improved by using a smaller incremental size in frequency (currently 0.1 MHz) and in degrees X rotation (currently 1 degree) in principle, however this would need more computational time and power.

These findings emphasize the importance of selecting the appropriate in-plane rotation for optimizing SAW device performance. Further investigation into M-IDT and fluidics at various rotations can refine the optimization of fluidic streaming in these devices.

The wave fields generated by a single trapezoidal IDT, oriented at angles 0°, 30°, 60°, and 90° with respect to the X-direction, were simulated to assess their interactions with droplets and determine the influence of different wave modes on the fluid
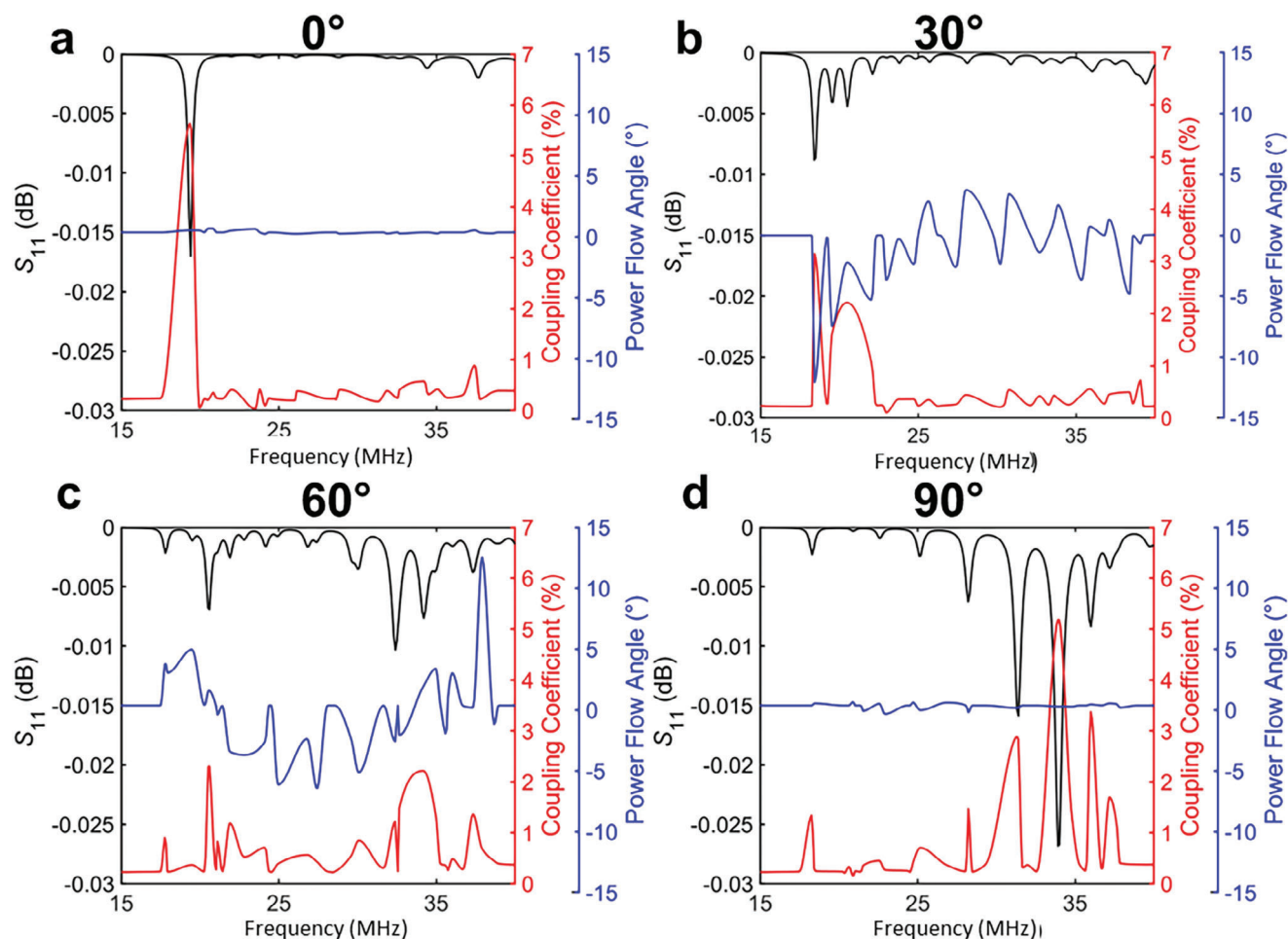
**ADVANCED
SCIENCE NEWS**

www.advancedsciencenews.com

**ADVANCED
FUNCTIONAL
MATERIALS**

www.afm-journal.de

Figure 4. Simulated wave modes properties (S_{11}, coupling coefficient, and power flow angle) with respect to Frequency for rotation angles a) 0°, b) 30°, c) 60°, and d) 90°.

(**Figure 5**). The selected frequencies – 19.8 MHz, 18.6 MHz, 32.2 MHz, and 34.4 MHz for angles 0°, 30°, 60°, and 90°, respectively – correspond to the lowest S_{11} minima per angle, ensuring optimal energy conversion.

The maximum displacement amplitudes of wavefields align with the frequencies with the highest coupling coefficients and lowest S_{11} minima. For 0° at 19.8 MHz and 30° at 18.6 MHz, the R-SAW beam profiles show the straight-lined patterns of peaks and troughs that are confined to the surface, characteristic of SAW. In contrast, at higher frequencies (32.2 MHz for 60° and 34.4 MHz for 90°), the distortion of the beam profiles indicates excitation within the substrate, as evidenced by the penetration of waves into the substrates thickness, thereby interfering with the surface waves.[9]

Moreover, the simulated wavefield displacement in the XY plane confirms the calculated power flow angles. In the case of 0° and 90° (Figure 5a,d), an almost ideal symmetry with respect to the beam axis was observed. As no beam steering occurs, the power flow is parallel to the SAW propagation direction. For 30° and 60° cases at 18.6 MHz and 32.2 MHz (Figure 5b,c), respectively, no symmetry is observed due to the beam steering. The beam profiles indicate a slight focusing effect, i.e., the width of

the SAW beam profile decreases with increasing distance from the IDT. This is likely caused by diffraction effects due to the limited aperture of the IDTs.[9]

Figure 5 also illustrates the wavefield droplet interaction, displaying the acoustic velocity (mm s^{-1}). It is observed that R-SAW enters the droplet at approximately the R-SAW angle. However, this is not the case for the higher frequency modes. Instead, the higher acoustic velocity is distributed throughout the droplet, indicating a different mechanism of fluid actuation.

Illustrating the wave mode shape is useful for understanding the behavior of the SAW on the 128° YX-cut LiNbO$_3$ substrate (**Figure 6a**). Note that eigenmode studies cannot be used to measure the displacement amplitudes;[46] hence, the colors are shown for visual demonstration of the shapes and are not to a particular scale. The white arrows indicate the direction of moment of the different wave types.

Figure 6a highlights the distinct surface component and vertical displacement characteristic of R-SAW at X- rotations 0° and 30°. In contrast, the wave modes at 60° and 90° have both vertical and horizontal displacements, indicative of non-pure modes that combine elements of R-SAW and SH-SAW. This blending of
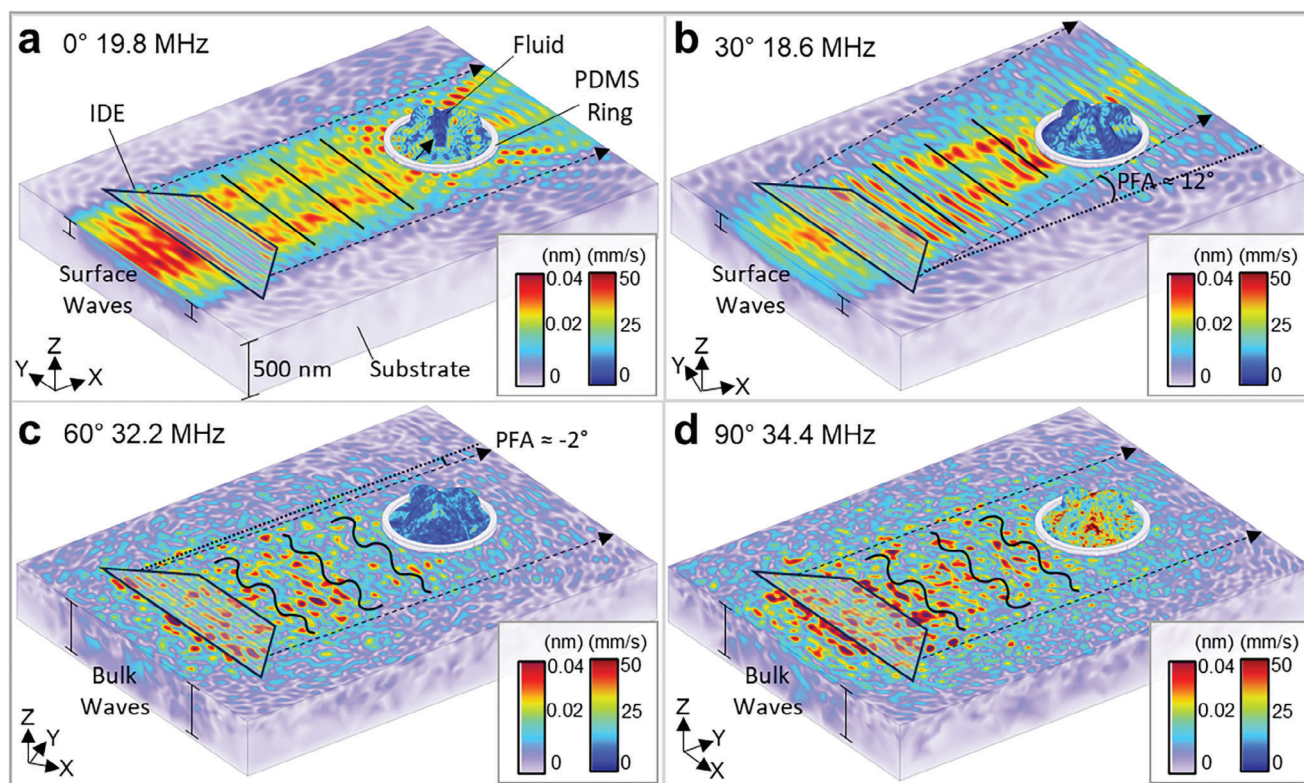
**ADVANCED
SCIENCE NEWS**

www.advancedsciencenews.com

**ADVANCED
FUNCTIONAL
MATERIALS**

www.afm-journal.de

Figure 5. 3D simulation of key wavefields and their interaction with fluid. a) 0° at 19.8 MHz b) 30° at 18.6 MHz c) 60° at 32.2 MHz d) 90° at 34.4 MHz.

wave modes suggests the presence of P-SH-SAWs, with 60° and 90° displaying varying ratios of these mixed modes.

The analysis suggests that the optimal wave modes for acoustofluidic applications on 128° YX-cut LiNbO$_3$ substrate, within the 15 to 40 MHz frequency range, are R-SAW and P-SH-SAW. Specifically, R-SAW dominates and is the most effective at rotation angles between 0° and 30°, while P-SH-SAW becomes more prominent and advantageous at angles between 60° and 90°. Figure 6b visually summarizes the optimal wave modes for this substrate across different angles, illustrating that R-SAW is optimal at angles near 0°, while P-SH-SAW is most effective at angles near 90°. The angles in-between, in the grey area, are typically a combined mode which have lower coupling efficiency.

Brodie et al.[27] studied SH-SAW using 36° Y-X LiTaO$_3$ and observed that the induced boundary pressure oscillations resulted in higher streaming velocities compared to R-SAW. This finding aligns with the results presented in Figure 5d, validating the effects due to SH-SAW component. Likewise, Figure 6c shows the R-SAW and P-SH-SAW propagating along the length of the substrate demonstrating the shear-horizontal component of the wave within the bulk as well as the vertical component on the surface. Orientations 30° and 60° are not depicted in Figure 6c because representing these angles requires a 3D rotation, which extends beyond the 2D capabilities of Euler angles with COMSOL.

Figure 6d displays the Z displacement for each mode demonstrating that the R-SAW is almost double in magnitude which validates those shown in Figure 4d. Furthermore, the observed

phenomenon of P-SH-SAW streaming is intriguing given the minimal attenuation of the SH-wave when interacting with fluid.[27] This unexpected behavior can be attributed to the reduced Z displacement inherent in SH-SAW, hindering efficient momentum transfer to the fluid. Numerical modelling (Figure 2d and Figure 6d) demonstrates that the P-SH-SAW Z displacement is ≈40% that of R-SAW Z displacement, making it unlikely to solely account for the increased streaming velocities.[27] Wave modes with lower Z displacement, such as SH-SAW, can be advantageous for biosensing applications, where minimal fluid perturbation is required. Figure S12 in the Supporting Information provides further displacement insights of such modes by illustrating variation of X and Y displacements with frequency.

Brodie et al.[27] propose a mechanism involving the entrapment of a thin visco-elastic fluid layer for shear wave polarized devices, which has a decay length of $\delta = \sqrt{\frac{2\eta}{\omega\rho}}$, where η is the shear viscosity of the liquid and ρ is the density of the liquid, and ω is the angular frequency.[27,47,48] The oscillation of this layer generates a small pressure difference relative to the surrounding liquid, attributable to the compression wave formed at the droplet boundary. The resultant oscillation of this boundary pressure generates to acoustic waves.

Figure 7 shows the simulated streaming mechanisms for both (a) R-SAW and (b) P-SH-SAW. The PDMS ring was excluded to provide a clear visualization of the wave mode contributions and their interactions. The top images depict displacement and pressure distribution, and the bottom images show the laminar flow velocities, with the scale values capped for comparison purposes.
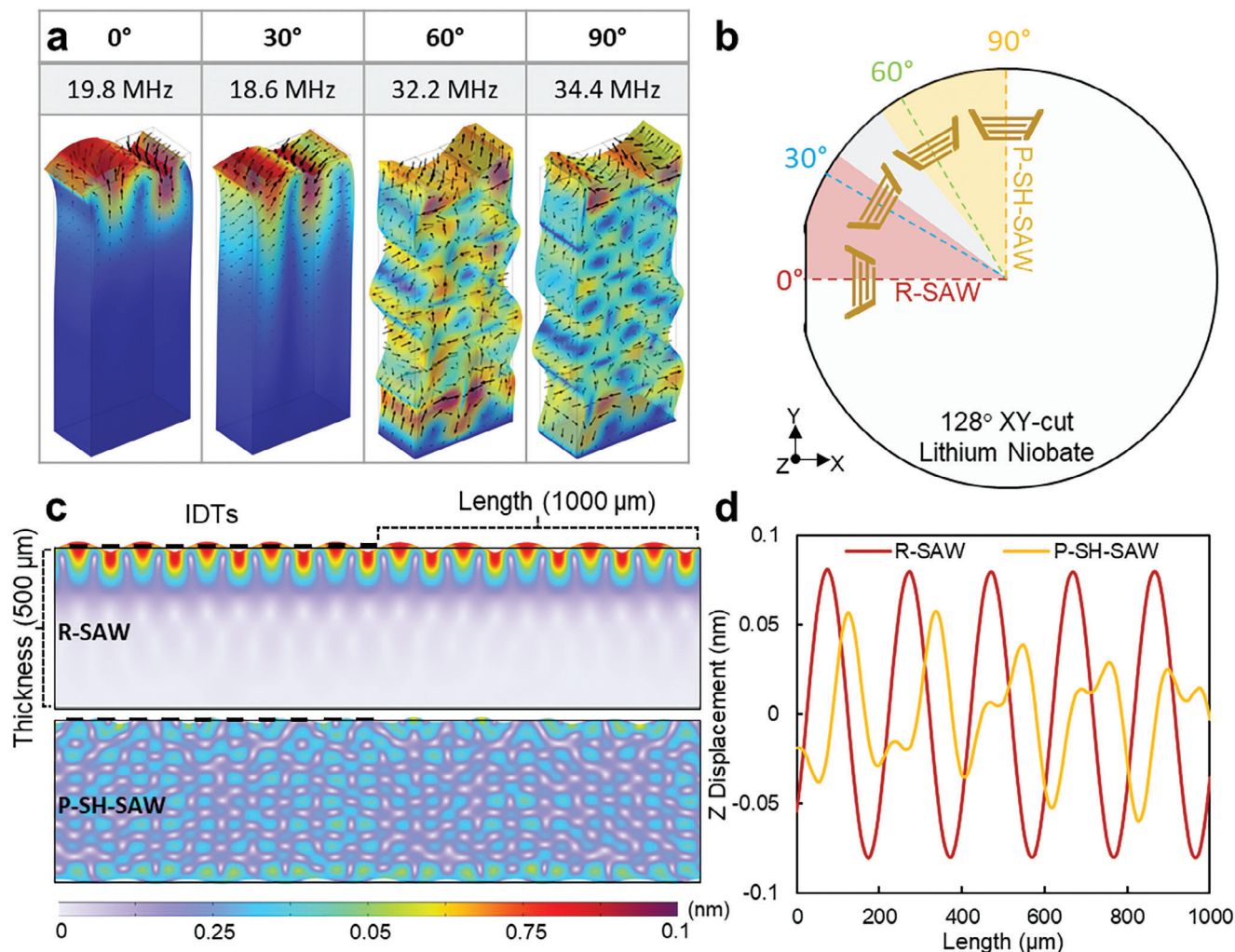
Figure 6. a) Eigenmode shape for the key frequency at each angle. Black arrows demonstrating displacement direction. b) Key wave modes around the 128° YX-cut LiNbO$_3$ substrate. c) 2D side view R-SAW displacement (top) and P-SH-SAW (bottom) (d) Z displacement along the length (1000 μm) for both R-SAW (red) and P-SH-SAW (orange).

In Figure 7a, the R-SAW (red highlight) surface displacement enters the droplet at the R-SAW angle ($\theta_R = \approx 22°$). Figure 7b similar displays the influence of R-SAW and highlights the SH-SAW (green highlight) pressure difference at the boundary, which results in significant boundary laminar flow velocities at an angle of $\theta_{SH} = 90°$. Interestingly, vertical cross-section patterns atypical for SH-SAW are observed, confirming the hybrid nature of P-SH-SAW (orange highlight) due to the combination of R-SAW and SH-SAW.

The streaming patterns for both R-SAW and P-SH-SAW modes, as indicated by the white arrows, are notably similar. However, the P-SH-SAW has minimal damping in the liquid compared to the R-SAW, due to the pivotal role of boundary layer oscillations in driving the streaming phenomena.[27] This reduced damping effect could be an advantage in applications involving larger or more viscous fluid volumes or in scenarios requiring wave propagation through additional materials.

4.2. Experimental Verifications

The S_{11} of the M-IDT was measured at IDT-oriented angles of 0°, 30°, 60°, and 90° with respect to the X-direction (**Figure 8a**). The S_{11} results correlated well with the simulated values, with the lowest S_{11} minima occurring 90°, followed by the R-SAW at 0°. Given the strong relationship between the coupling coefficient and S_{11} minima, these results indicate that certain wave modes could be advantageous. However, despite high coupling coefficients, some wave modes, such as pure-SH-SAW, may be less effective for fluidic streaming due to their predominant horizontal displacements, which limits fluid interaction.[13,27,44] As a result, these wave modes are typically better suited for sensing applications rather than fluid streaming. Nevertheless, previous simulations suggest that a combination of wave modes incorporating Z displacement could enhance acoustofluidic effects. Consequently, experimental verifications of the acoustofluidics effects of these wave modes were undertaken.
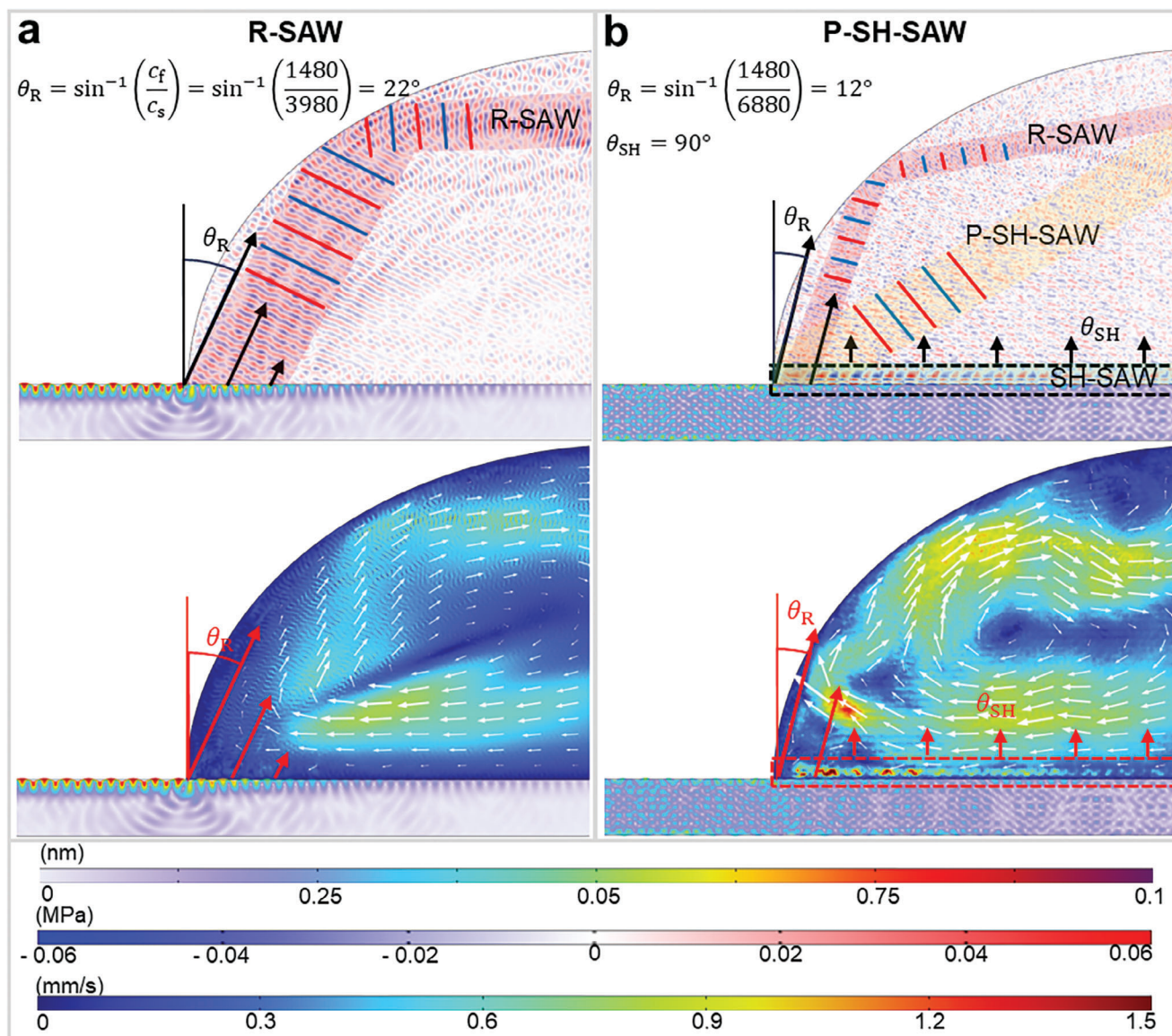
**ADVANCED
SCIENCE NEWS**

www.advancedsciencenews.com

**ADVANCED
FUNCTIONAL
MATERIALS**

www.afm-journal.de

Figure 7. Streaming mechanism for a) R-SAW and b) P-SH-SAW. The top images show the displacement and pressure distribution. The wave mode contributions are highlighted showing R-SAW (red), SH-SAW (green), and P-SH-SAW (orange). The bottom images show displacement and laminar flow velocity. The white arrows indicate the streaming direction inside the droplet.

The M-IDT was utilized for conducting fluid actuation tests frequencies corresponding to the three most prominent S_{11} minima, across different X rotation angles (0°, 30°, 60°, and 90°). Average area streaming velocity—defined as the mean velocity of fluid particles across a specified area induced by the acoustic waves—was measured during these tests, as shown in Figure 8b. The results reveal a strong correlation between the average area streaming velocities and the measured S_{11} minima. Notably, at 90° rotation, each frequency (31.3 MHz, 34.4 MHz, and 36.6 MHz) achieved comparable average area velocities ($\approx$ 1.19 mm s^{-1}, 1.58 mm s^{-1}, and 1.33 mm s^{-1}, respectively) to that of R-SAW at 0° 19.8 MHz ($\approx$1.35 mm s^{-1}). It is probable that those 3 frequencies at 90° rotation have R-SAW and SH-SAW components. Among the 90° wave modes, the 34.4 MHz had the

highest acoustic streaming, which correlates with its larger Z displacement of $\approx$0.034 nm (compared to other Z displacements at 90°) and a lower S_{11} of −13.4 dB. At 90° 31.3 MHz, the Z displacement measured $\approx$0.02 nm, higher than the 0.01 nm at 90° 36.6 MHz, yet the latter offered a higher S_{11} of −9.8 dB compared to −6.7 dB. The reflection coefficient signifies how much of the input power reflected to the input port of the device; therefore, the 90° 36.6 MHz frequency proved more efficient than 31.3 MHz, which explained its superior average acoustic streaming velocity. At P-SH-SAW 34.4 MHz, the average area velocity magnitude was increased by $\approx$15% compared to 0° R-SAW. Despite the lesser Z displacement (0.034 nm) of P-SH-SAW 34.4 MHz compared to 0° R-SAW (0.09 nm), the former had a larger S_{11} minima of −13.4 dB compared to −8.2 dB. Nonetheless, both R-SAW at 0°
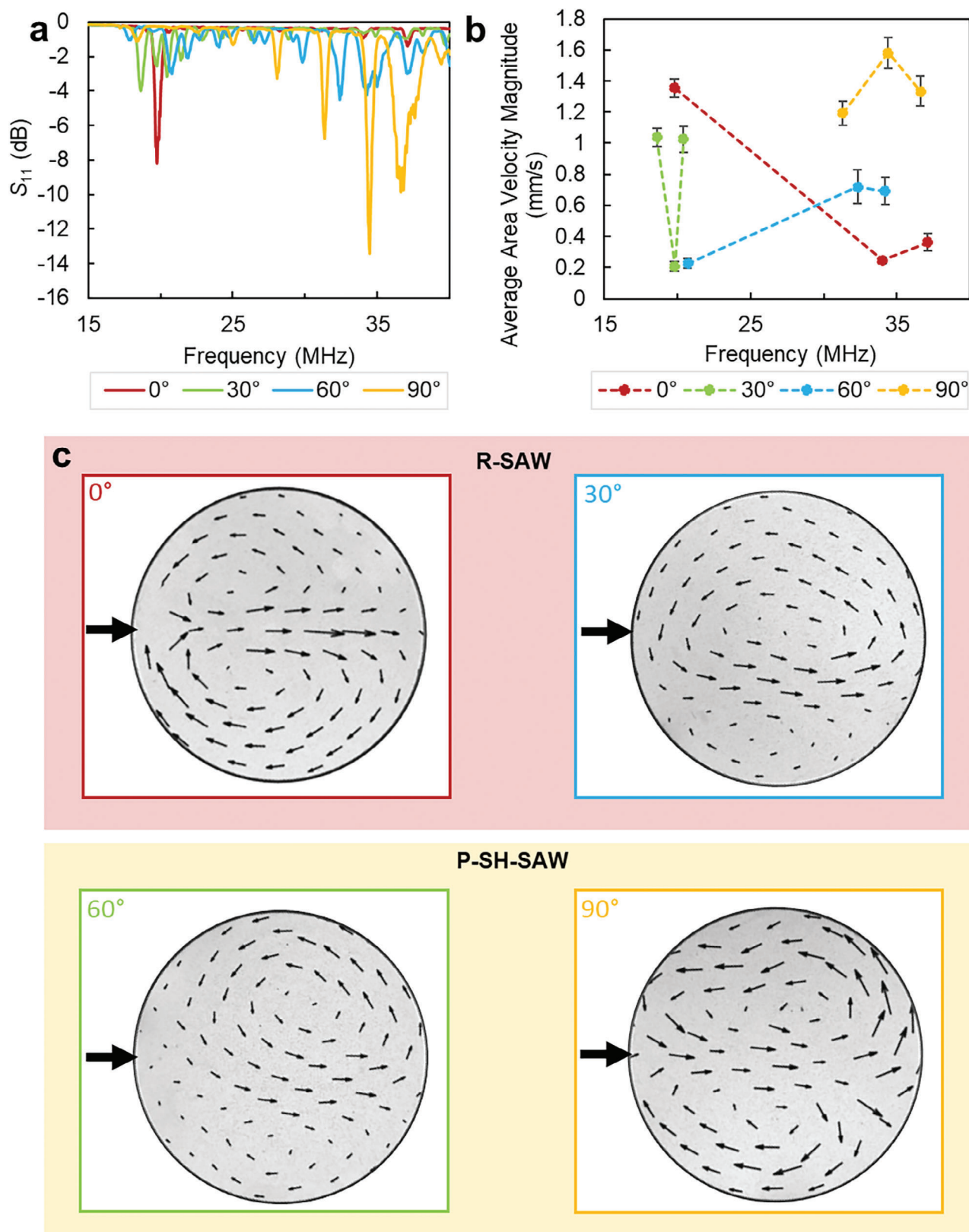
Figure 8. a) Measured S_{11} values for X rotation angles 0°, 30°, 60°, and 90° ($n = 6$) b) Measured average area velocity magnitude for the largest three S_{11} minima frequencies for each angle. ($n = 5$). The data is represented as mean $\pm$ s.d. c) Corresponding experimental streaming patterns for optimal frequencies / wave modes (0° at 19.8 MHz, 30° at 18.6 MHz, 60° at 32.2 MHz, and 90° at 34.4 MHz.). The 100 µL fluid (50:50, water: glycerol) within a PDMS ring was actuated at 30 dBm (1 W).

and SH-SAW at 90° demonstrated notably higher streaming velocities compared to other angles and frequencies.

The average area velocities at 30° rotation were measured at 1.04 mm s⁻¹ and 1.03 mm s⁻¹ for frequencies 18.6 MHz and 20.5 MHz, respectively. While slower than the velocities at 0° R-SAW, they outperformed the 60° P-SH-SAW of ≈0.72 mm s⁻¹ (32.3 MHz) and 0.69 mm s⁻¹ (34.2 MHz). Nonetheless, both angles still offer viable acoustic streaming velocities for acoustofluidic applications. The decline in 60° P-SH-SAW average area acoustic streaming velocity corresponds with the reduced Z displacement (≈0.014 nm for both) and S_{11} values (4.5 dB and 4 dB) compared to 90° P-SH-SAW at 34.4 MHz. Despite equivalent Z displacement with 90° 36.6 MHz, the latter had significantly greater S_{11} minima (≈40%) and ≈30% greater average area acoustic streaming velocity. This highlights the potential of employing alternative angles using different wave modes for acoustofluidic applications, with the measured S_{11} minima serving as useful guidelines for utilizing other harmonics. Overall, P-SH-SAW emerges as a valuable tool for actuation in acoustofluidics, facilitating opportunities for simultaneous sensing and actuation.

Experimental results show that distinct streaming patterns were generated for each angle: 0° at 19.8 MHz, 30° at 18.6 MHz, 60° at 32.2 MHz, and 90° at 34.4 MHz (Figure 8c). Variations in these streaming patterns may originate from differences in power flow angles. At 0° and 90°, where the power flow angle is 0°, a butterfly-shape streaming pattern occurs with the wave propagating through the center. Notably, the R-SAW double vortex exhibits stagnant regions near the IDT actuation, with the highest acoustic streaming velocity in the center of the droplet where the wave is propagating through. Whereas the P-SH-SAW's double vortex has stagnant regions further from the IDT, with highest acoustic streaming at the droplet's boundary, likely due to reduced damping. This pattern holds true for the 30° R-SAW and 60° P-SH-SAW configurations. Conversely, at 30° and 60°, with power flow angles of ≈12.1° and 2.2° respectively, one vortex appears larger than the other, possibly due to an offset in the propagating wave. Therefore, the beam steering plays a critical role in particle control by redistributing wave energy, which directly affects vortex size and symmetry in the streaming patterns. These power flow angles were validated in the simulations as depicted in Figure 4 and Figure S8 (Supporting Information). However, other factors may influence streaming patterns, and future research utilizing a laser vibrometer could provide further validation of power flow angles. However, for hybrid wave modes, laser vibrometer captures only surface displacements, not bulk movements, making beam steering quantification more challenging.

Further exploration was undertaken to delve into the damping phenomena within the fluid medium. It is well-established that SH-SAW experiences significantly less attenuation when penetrating the liquid compared to R-SAW.[27] However, there is evidence suggesting that some attenuation does occur due to both in-plane, normal and parallel to surface components.[49] To better understand how viscosity influences these effects, **Figure 9a** presents the average area velocity magnitude of R-SAW and P-SH-SAW fluid actuation at 20 dBm (0.1 W) across different viscosities. The results reveal that at lower viscosities, P-SH-SAW exhibits average area viscosity values exceeding those of R-SAW

by over 50%. The P-SH-SAW component demonstrates a velocity magnitude reduction of 55% with increasing viscosity, while R-SAW experiences a reduction of 42%. These findings show that the damping effect exists with the P-SH-SAW component when increasing the viscosity. This phenomenon is likely attributable to the high viscosity impacting the R-SAW component (Z displacement) of the P-SH-SAW. Nevertheless, the SH-SAW component continues to contribute effective boundary layer streaming.

Additionally, Figure 9b shows the average area velocity at varying powers while maintaining a viscosity ratio of 60:40 (water: glycerol). Both wave modes display a consistent linear increase in average area velocity magnitude, with P-SH-SAW consistently outperforming R-SAW by 50%. Despite the influence of viscosity on P-SH-SAW, macro-streaming is demonstrated within a 1 mL fluid volume PDMS ring. Figure 9c captures the initial frame (t = 0), where particles are pipetted into the fluid for visualization purposes. Within just two seconds, P-SH-SAW propagates through the entire 1 mL sample (25 mm diameter), leaving a distinct clear central line. In contrast, within the same timeframe, R-SAW induces only minimal fluid movement. Since the boundary layer oscillation is also responsible for the P-SH-SAW streaming, less damping would be expected.

Using culture plates, like 96-well plates, for SAW applications enhances standardization, scalability, and biocompatibility while integrating seamlessly into lab workflows.[50] This approach also reduces contamination risk, is cost-effective, and provides greater versatility for various experimental conditions.[51] The P-SH-SAW wave mode was applied to a single 96-well culture plate coupled with a droplet layer of glycerol (**Figure 10a**). The previous investigations have shown P-SH-SAW to be highly effective in manipulating large fluid volumes and high-viscosity liquids, demonstrating its ability to maintain efficient energy transfer with minimal damping. This makes it particularly well-suited for driving acoustic streaming within the well plate. In this setup, the glycerol acts as a coupling medium that transfers the acoustic energy from the piezoelectric substrate through the culture plate to the fluid. The acoustic waves travel through the solid-liquid interface, creating fluid motion and acoustic streaming.

The average area velocity magnitude at various powers for both P-SH-SAW and R-SAW is shown in Figure 10b, focusing on an area segment (2D top-view) of the culture plate fluid (as shown in the area and scale depicted in Figure 10c). P-SH-SAW demonstrates a significantly higher streaming velocity of ≈1.2 mm s⁻¹, outperforming the R-SAW, which fails to generate any streaming through the culture plate at 1 W (30 dBm). This discrepancy can be attributed to the wave modes different mechanisms. R-SAW demonstrates poor performance in this context due to its high damping when interacting with the glycerol droplet and well plate. In contrast, enhanced streaming is due to P-SH-SAWs efficient interaction with the fluid through the boundary layer oscillations and minimal damping, leading to improved streaming behavior.

Overall, these results demonstrate the effectiveness of using P-SH-SAW within culture plates, suggesting significant potential for various biological applications. For instance, it can be utilized for mixing to ensure uniform cell exposure to nutrients and factors, as well as facilitating non-enzymatic cell detachment offering a gentler method of harvesting.[52–54]
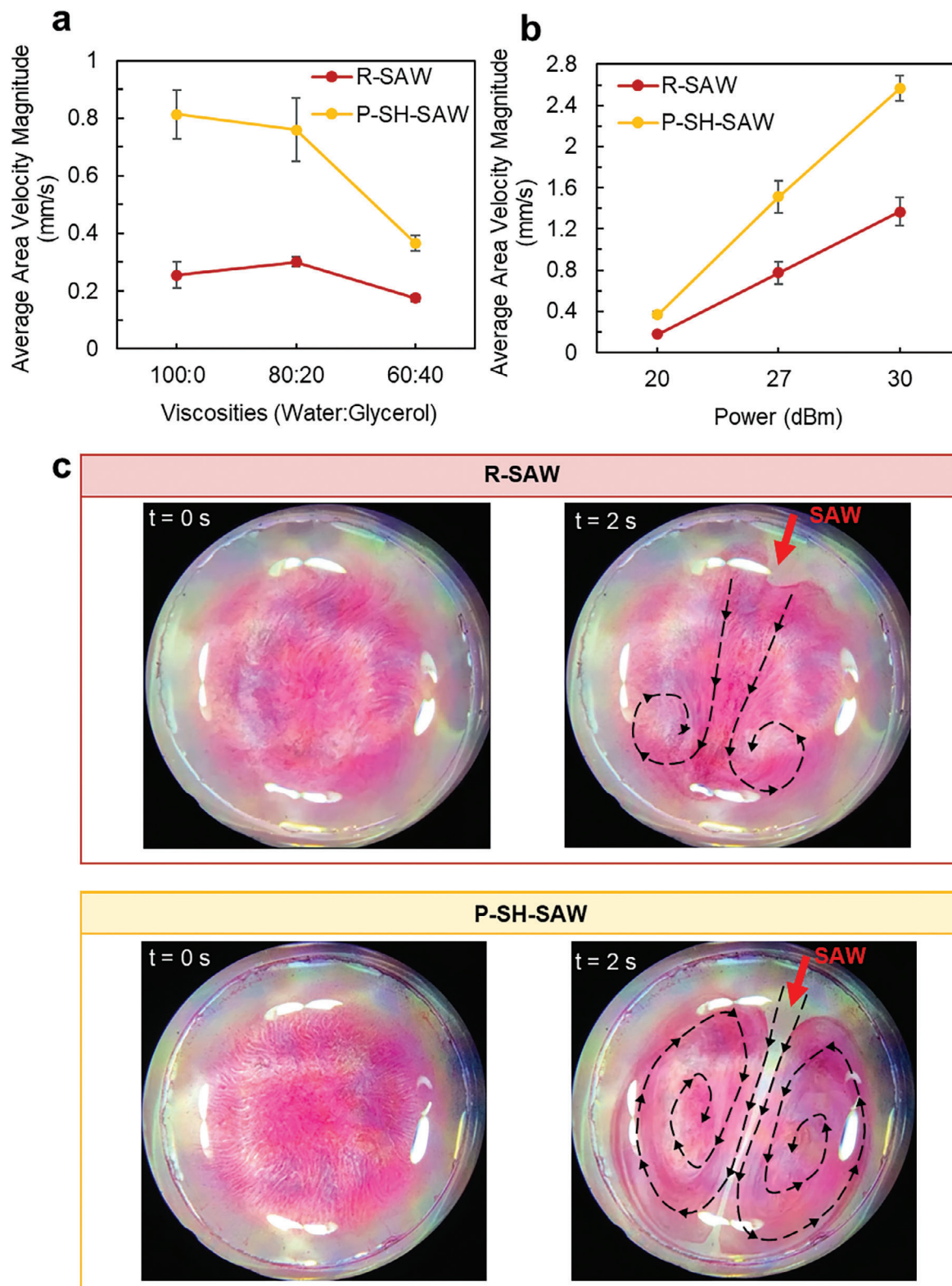
**ADVANCED
SCIENCE NEWS**

www.advancedsciencenews.com

**ADVANCED
FUNCTIONAL
MATERIALS**

www.afm-journal.de

Figure 9. Average area velocity magnitude for 0° R-SAW and 90° P-SH-SAW for different a) viscosity fluids (water: glycerol ratio) ($n = 5$) b) IDT power (20 dBm (0.1 W), 27 dBm (0.5 W), and 30 dBm (1 W)) ($n = 5$). All data is represented as mean ± s.d. c) Large 1 mL fluid volume (PDMS ring diameter 25 mm) showing at t = 0 and t = 2 s with black arrows indicating the streaming pattern.

**ADVANCED
SCIENCE NEWS**

www.advancedsciencenews.com

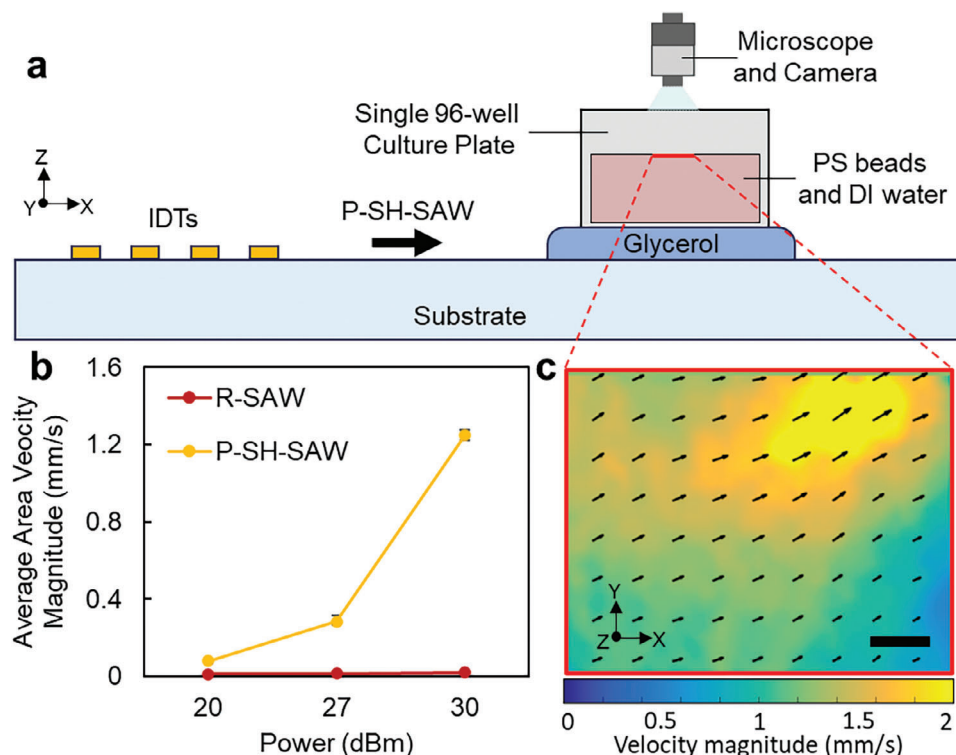**ADVANCED
FUNCTIONAL
MATERIALS**

www.afm-journal.de

Figure 10. Streaming in a culture plate coupled with glycerol. a) 2D device set-up with a glycerol layer coupling a single 96-well culture plate. b) Average area velocity magnitude for 0° R-SAW and 90° P-SH-SAW inside a culture plate at different powers ($n = 3$). The data is represented as mean ± s.d. c) 2D top view PIVLab image of the streaming velocity magnitude for 90° P-SH-SAW inside a culture plate at 30 dBm. Scale represents 0.25 mm.

5. Conclusion

This paper uses the multidirectional and reconfigurable M-IDT device to study alternative rotation angles and wave modes of the conventional 128^0 XY-cut LiNbO$_3$ for acoustofluidic actuation, aiming to broaden the scope of possibilities in acoustofluidics. By exploring orientation angles beyond the conventional 0°, we unlock diverse configurations such as maneuvering around obstacles, detecting into features, and enabling simultaneous multi-angle actuation.[8] Through COMSOL simulations of a unit cell, we characterized a large range of wave modes and calculated their coupling coefficient and power flow angles. Subsequent 2D and 3D COMSOL simulations validated these findings and demonstrated the interaction between the wavefield and fluidic environment. Utilizing the M-IDT with two simple reconfigurable arrangements, we examined wave mode fluid interactions at rotation angles of 0°, 30°, 60°, and 90°. We discovered a P-SH-SAW based streaming mechanism on the 128° YX-cut LiNbO$_3$. This method effectively combines R-SAW and SH-SAW components, offering a significant Z displacement (40% of the dominant R-SAW) alongside advantageous large boundary layer streaming with minimal damping. The P-SH-SAW achieved comparable streaming velocities to R-SAW at 30 dBm, with a 100 µL (50:50, water: glycerol ratio) sample. Notably, damping experiments demonstrated the influence of viscous damping P-SH-SAW performance, yet P-SH-SAW acoustic streaming still surpassed that of R-SAW. This highlights the considerable promise of P-SH-SAW in both macro- and micro- scale acoustic stream-

ing compared to R-SAW. Furthermore, P-SH-SAW demonstrated its utility in generating streaming flow in a culture plate, showcasing its potential for real-world applications with standardized and biocompatible equipment. Additionally, the rapid streaming of P-SH-SAW at different viscosities shows the potential for integrating bio-sensing and fluid manipulation on a single substrate. Overall, the M-IDT platform offers significant potential for advancing acoustofluidics. Future work could explore alternative substrates like 36° YX-cut LiTaO$_3$, varied fluid vessel designs, and alternative IDT configurations, including multi-frequency or asymmetric designs. Investigating the simultaneous operation of multiple IDTs could enable complex wave interactions, multidirectional wavefields, and tailored streaming profiles, opening new avenues for innovative research and prototyping of multifunctional acoustofluidic systems.

Supporting Information

Supporting Information is available from the Wiley Online Library or from the author.

Conflict of Interest

The authors declare no conflict of interest.

Data Availability Statement

The data that supports the findings of this study are available from the corresponding author upon reasonable request.

[1] X. Ding, P. Li, S. C. S. Lin, Z. S. Stratton, N. Nama, F. Guo, D. Slotcavage, X. Mao, J. Shi, F. Costanzo, T. J. Huang, *Lab Chip* **2013**, *13*, 3626.
[2] A. V. Mamishev, K. Sundara-Rajan, F. Yang, Y. Du, M. Zahn, *Proc. IEEE* **2004**, *92*, 808.
[3] M. B. Mazalan, A. M. Noor, Y. Wahab, S. Yahud, W. S. W. K. Zaman, *Micromachines* **2021**, *13*, 30.
[4] R. Fogel, J. Limson, A. A. Seshia, *Essays Biochem* **2016**, *60*, 101.
[5] M. P. Nair, A. J. T. Teo, K. H. H. Li, *Micromachines* **2021**, *13*, 24.
[6] Y. Q. Fu, J. K. Luo, N. T. Nguyen, A. J. Walton, A. J. Flewitt, X. T. Zu, Y. Li, G. McHale, A. Matthews, E. Iborra, H. Du, W. I. Milne, *Prog. Mater. Sci.* **2017**, *89*, 31.
[7] S. Song, Q. Wang, J. Zhou, A. Riaud, *Nanotechnol. Precis. Eng.* **2022**, *5*, 035001.
[8] N. Zhang, J. Mei, T. Gopesh, J. Friend, *IEEE Trans. Ultrason. Ferroelectr. Freq. Control* **2020**, *67*, 2176.
[9] A. w. R. Weser, S. m. M. Weihnacht, *Ultrasonics* **2020**, *106*, 106160.
[10] M. Stringer, Z. Zeng, X. Zhang, Y. Chai, W. Li, J. Zhang, H. Ong, D. Liang, J. Dong, Y. Li, Y. Q. Fu, X. Yang, *Appl. Phys. Rev.* **2023**, *10*, 011315.
[11] Y. Wang, X. Li, H. Meng, R. Tao, J. Qian, C. Fu, J. Luo, J. Xie, Y. Q. Fu, *ACS Appl. Mater. Interfaces* **2024**, *16*, 45119.
[12] Y. Q. Fu, H. F. Pang, H. Torun, R. Tao, G. McHale, J. Rebound, K. Tao, J. Zhou, J. Lou, D. Gibson, J. Luo, P. Hu, *Lab Chip* **2021**, *21*, 254.
[13] H. F. Pang, R. Tao, J. Luo, X. Zhou, G. McHale, J. Rebound, H. Torun, D. Gibson, K. Tao, H. Chang, Y. Q. Fu, *Surf. Coat. Technol.* **2022**, *442*, 128336.
[14] G. Feng, L. Peng, B. F. Jarrod, M. Zhangming, Z. Hong, L. SIxing, N. Nitesh, R. F. James, J. B. Stephen, H. Tony Jun, *Proc. Natl. Acad. Sci. USA* **2015**, *112*, 43.
[15] C. Devendran, N. R. Gunasekara, D. J. Collins, A. Neild, *RSC Adv.* **2016**, *6*, 5856.
[16] J. Shi, D. Ahmed, X. Mao, S.-C. S. Lin, A. Lawit, T. J. Huang, *Lab Chip* **2009**, *9*, 2890.
[17] A. Ozcelik, J. Rufo, F. Guo, Y. Gu, P. Li, J. Lata, T. J. Huang, *Nat. Methods* **2018**, *15*, 1021.
[18] D. J. Collins, B. Morahan, J. Garcia-Bustos, C. Doerig, M. Plebanski, A. Neild, *Nat. Commun.* **2015**, *6*, 8686.
[19] J. Li, A. Crivoi, X. Peng, L. Shen, Y. Pu, Z. Fan, S. A. Cummer, *Commun. Phys.* **2021**, *4*, 113.
[20] Y. Wang, H. Pan, D. Mei, C. Xu, W. Weng, *Lab Chip* **2022**, *22*, 1149.
[21] R. O'Rorke, A. Winkler, D. Collins, Y. Ai, *RSC Adv.* **2020**, *10*, 11582.
[22] A. R. Rezk, J. K. Tan, L. Y. Yeo, *Adv. Mater.* **2016**, *28*, 1970.
[23] W. Huang, Q. Yang, J. Liao, S. Ramadan, X. Fan, S. Hu, X. Liu, J. Luo, R. Tao, C. Fu, *Biosens. Bioelectron.* **2024**, *247*, 115944.
[24] M. Agostini, F. Lunardellim, M. Gagliardi, A. Miranda, L. Lamanna, A. G. Luminare, F. Gambineri, M. Lai, M. Pistello, M. Cecchini, *Adv. Funct. Mater.* **2022**, *32*, 2201958.
[25] Y. Hur, J. Han, J. Seon, Y. E. Pak, Y. Roh, *Sens. Actuators Phys.* **2005**, *120*, 462.
[26] S. Li, Y. Wan, Y. Su, C. Fan, V. R. Bhethanabotla, *Biosens. Bioelectron.* **2017**, *95*, 48.
[27] D. S. Brodie, Y. Q. Fu, Y. Li, M. Alghane, R. L. Reuben, A. J. Walton, *Appl. Phys. Lett.* **2011**, *99*, 153704.
[28] C. Fu, *Appl. Phys. Lett.* **2017**, *110*, 173501.
[29] M. Alghane, B. X. Chen, Y. Q. Fu, Y. Li, J. K. Luo, A. J. Walton, *J. Micromechanics Microengineering* **2010**, *21*, 015005.
[30] P. Dumčius, R. Mikhaylov, X. Zhang, M. Bareford, M. Stringer, R. Errington, C. Sun, E. Gonzalez, T. Krukoyski, J. M. Falcon-Perez, D. Liang, Y. Q. Fu, A. Clayton, X. Yang, *Small* **2023**, *19*, 2300390.
[31] A. Tarasenko, R. Čtvrtlík, R. Kudělka, *Sci. Rep.* **2021**, *11*, 2845.
[32] K. Uchino, in *Advanced Piezoelectric Materials*, (Ed.: K. Uchino), Woodhead Publishing, Cambridge **2010**, pp. 1–85.
[33] V. I. Anisimkin, *IEEE Trans. Ultrason. Ferroelectr. Freq. Control* **2014**, *61*, 120.
[34] J. F. Pazos-Ospina, J. L. Ealo, E. E. Franco, *J. Acoust. Soc. Am.* **2017**, *142*, 61.
[35] J. Huang, X. Ren, Q. Zhou, J. Zhou, Z. Xu, *Ultrasonics* **2023**, *128*, 106865.
[36] R. Mikhaylov, M. Stringer, P. Dumcius, H. Wang, F. Wu, X. ZHang, V. Akhimien, C. SUn, A. Clayton, Y. Q. Fu, L. Ye, Z. Dong, Z. Wu, X. Yang, *J. Micromechanics Microengineering* **2021**, *31*, 074003.
[37] C. Sun, R. Mikhaylov, Y. Q. Fu, F. Wu, H. WAng, X. Yuan, Z. Xie, D. Liang, Z. Wu, X. Yang, *IEEE Trans. Electron Devices* **2021**, *68*, 393.
[38] R. Mikhaylov, Fu. Wu, H. Wang, A. Clayton, C. SUn, Z. Xie, D. Liang, Y. Dong, F. Yuan, D. Moschou, Z. Wu, M. H. Shen, J. Yang, Y. Q. Fu, Z. Yang, C. Burton, R. Errington, M. Wiltshire, X. Yang, *Lab Chip* **2020**, *20*, 1807.
[39] A. Riaud, M. Baudoin, O. Bou Matar, J.-L. Thomas, P. Brunet, *J. Fluid Mech.* **2017**, *821*, 384.
[40] R. J. Adrian, *Annu. Rev. Fluid Mech.* **1991**, *23*, 261.
[41] W. Thielicke, R. Sonntag, Particle Image Velocimetry for MATLAB: Accuracy and enhanced algorithms in PIVlab **2021**, *9*, 12.
[42] S. Kim, B. Prasad, J. Kim, *J. Korean Soc. Vis.* **2016**, *14*, 38.
[43] A. Smirnov, V. Anisimkin, E. Shamsutdinova, P. Li, H. Ezzin, Z. Qian, T. Ma, I. Kuznetsova, *Sensors* **2022**, *22*, 7231.
[44] D. Mandal, S. Banerjee, *Sensors* **2022**, *22*, 820.
[45] A. S. Koigerov, A. V. Korlyakov, *Russ. Microelectron.* **2022**, *51*, 226.
[46] Eigenfrequency Analysis, https://www.comsol.com/multiphysics/eigenfrequency-analysis (accessed: November 2023).
[47] S. J. Martin, A. J. Ricco, T. M. Niemczyk, G. C. Frye, *Sens. Actuators* **1989**, *20*, 253.
[48] G. McHale, M. I. Newton, M. K. Banerjee, J. A. Cowen, *Mater. Sci. Eng. C* **2000**, *12*, 17.
[49] S. Ballandras, A. Reinhardt, A. Khelif, M. Wilm, V. Laude, W. Daniau, V. Blondeau-Patissier, *J. Appl. Phys.* **2006**, *99*, 054907.
[50] Z. Tian, *Sci. Adv.* **2020**, *6*, 0494.
[51] G. Greco, M. Agostini, I. Tonazzini, D. Sallemi, S. Barone, M. Cecchini, *Anal. Chem.* **2018**, *90*, 7450.
[52] A. Salari, S. Appak-Baskoy, I. R. Coe, S. S. H. Tsai, M. C. Kolios, *RSC Adv.* **2021**, *11*, 32824.
[53] Y. Kurashina, C. Imashiro, M. Hirano, T. Kuribara, K. Totani, K. Ohnuma, J. Friend, K. Takemura, *Commun. Biol.* **2019**, *2*, 393.
[54] C. Imashiro, M. Hirano, T. Morikura, Y. Fukuma, K. Ohnuma, Y. Kurashina, S. Miyata, K. Takemura, *Sci. Rep.* **2020**, *10*, 9468.